Probabilistic Stability Analysis of Fault-Initiated Islanding Microgrids Without Inertia

M.H.Roos, P.H.Nguyen, J.Morren, J.G.Slootweg

Department of Electrical Engineering, Eindhoven University of Technology, Eindhoven, the Netherlands. e-mail: m.h.roos@tue.nl

Abstract

Microgrids can be islanded to improve the reliability of the electrical energy supply during contingencies such as faults. It is still unclear what stability phenomena can occur in microgrids without inertia during and immediately after the fault-initiated islanding transient, and how the stability should be evaluated. To allow robust planning and operation, a stability analysis methodology should be able to take into account the inherent uncertainty of load and renewable energy sources. Therefore, this paper proposes a probabilistic stability analysis methodology for fault-initiated islanding of microgrids based on a thorough analysis of the root causes of instability during islanding transients. To perform stability analysis within reasonable time and allow control actions during operation, dynamical microgrid models in the dq reference frame are described and validated by comparing time-domain simulations results to previously validated component-based models. The stability analysis methodology is demonstrated in a case study of a generic microgrid. The instability phenomena and the dq microgrid models are successfully validated, and the results indicate that the stability analysis methodology can assist the microgrid operator to improve fault-initiated islanding capability in order to improve reliability of supply.

Keywords:
Power system stability, Microgrids, Stability analysis, Islanding, Inertia

1. Introduction

Society is becoming increasingly dependent on the electrical energy supply, which motivates the research towards more reliable and resilient electricity (distribution) networks. By designing distribution networks as grid-connected microgrids, grid operators can utilize fault-initiated islanding (FII) to increase the reliability and resilience in case of a contingency in the external grid such as a short-circuit fault [1, 2, 3, 4].

Instability may occur during the FII transient, and distributed energy resources (DERs) and loads in the microgrid may disconnect, causing instability after the FII transient as demonstrated in [5]. Therefore, FII stability should be taken into account when planning and operating a microgrid. During the planning of a microgrid the stability will be evaluated using a set of expected operating conditions, which should be reevaluated when the microgrid properties change (e.g. connection of new DERs or loads) during operation.

Due to the varying load and generation capacity of (renewable) DERs over time, a deterministic stability verdict i.e. a stability verdict based on the ”worst case” may underestimate the ability of microgrids to perform FII. In contrast, probabilistic approaches can provide insight in the probability of successful islanding to the microgrid operator. This allows the microgrid operator to decide whether to enable FII based on the required reliability. However, a probabilistic methodology to analyze FII stability is lacking in the literature.

Stability during grid-connected and islanded operation as well as planned islanding have been thoroughly researched by e.g. [6, 7, 8]. However, the analysis of stability phenomena during and immediately after the FII transient is limited in the literature. Stability after microgrid FII with a mix of synchronous machine-based and inverter-based DERs has been previously analyzed for some cases by [1, 2, 3], however a rigorous analysis of the stability phenomena and root causes for instability associated with FII is still lacking in the literature. The effects of inverter control

Preprints (www.preprints.org) | NOT PEER-REVIEWED | Posted: 31 May 2020 doi:10.20944/preprints202005.0498.v1

Nomenclature

$[x_{min}, x_{max}]$ Minimum and maximum condition values.
α VFD drop-off parameter.
$\alpha_\beta, \beta_\beta$ Shape parameters of Beta distribution.
δ Internal speed controller state.
γ DER internal PLL controller state.
μ_{log}, σ_{log} Shape parameters of Lognormal distribution.
ω Network frequency.
ω_c Droop controller low-pass filter bandwidth.
ω_m Induction machine rotational speed.
ω_n Nominal network frequency.
ϕ_q q-axis internal torque controller state.
ψ^* Induction machine flux reference.
ψ_n Nominal induction machine flux.
ψ_d, ψ_q dq-axis internal voltage controller states.
ψ_{sd}, ψ_{sq} dq-axis induction machine stator flux.
σ VFD input voltage angle.
θ_i Frequency estimated by PLL i.
$\tilde{I}^*_{ld}, \tilde{I}^*_{lq}$ dq-axis current reference after current limiting.
$\tilde{T}^*$ VFD torque reference after torque limiting.
ζ_d, ζ_q dq-axis internal current controller states.
C_{dc} DC-link capacitance.
C_f DER LCL filter capacitance
C_l Constant impedance load capacitance.
I Number of condition variables.
I_{bd}, I_{bq} dq-axis load input current i.e. the sum of the input current of the node.
I_{dc} DC-link current.
I_{ind}, I_{inq} dq-axis VFD input current.
I_{ld}, I_{lq} DER inverter output current.
I^*_{ld}, I^*_{lq} dq-axis current reference.
I_{lim} DER current magnitude limit.
I_{lined}, I_{lineq} dq-axis branch current.
I_{Lld}, I_{Llq} Constant impedance load inductor current.
I_{od}, I_{oq} dq-axis DER LCL filter output current.
I_{sd}, I_{sq} dq-axis induction machine stator current.
K, L Sets of stable and unstable conditions.
$K_{p\omega}, K_{i\omega}$ Speed controller P,I gains.
K_{pc}, K_{ic} Current controller P,I gains.
K_{pf} Flux controller P gain.
K_{ppll}, K_{ipll} PLL controller P,I gains.
K_{pt}, K_{it} Torque controller P,I gains.
K_{pv}, K_{iv} Voltage controller P,I gains.
L_c DER LCL filter grid side inductance.
L_{dc} DER scaled primary source series inductance.
L_f DER LCL filter inverter side inductance.
L_{line} Branch inductance.
L_l Constant impedance load inductance.
mp_i, nq_i Droop control parameters of DER i.
N Planning or operation conditions set.
n Current condition value of set N.
p Number of induction machine pole pairs.
P^*, Q^* DER active and reactive power references.
P_e Power absorbed by induction machine.
p_i Probability of condition i.
P_i, Q_i Active and reactive power output of DER i.
p_{ss} Sum of the probability of stable conditions.
r_c DER LCL filter grid side resistance.
R_{dc} DER scaled primary source series resistance.
r_f DER LCL filter inverter side resistance.
R_{line} Branch resistance.
R_l Constant impedance load resistance.
S_d dq-axis rectifier voltage coefficient.
T Planning or operation time horizon.
t Current time step of time horizon T
t_f, t_{gfi}, t_{gsi} Initiation time of fault, GFI and GSI stages.
T_{lim} VFD torque magnitude limit.
V_n Nominal network voltage.
V_{bid}, V_{biq} dq-axis voltage of node i.
V_{Cdc} DC-link capacitance voltage.
V_{cd}, V_{cq} dq-axis DER LCL filter capacitor voltage.
V_{cld}, V_{clq} Constant impedance load capacitor voltage.
V_{dc} DER scaled primary source voltage.
v_{id}, v_{iq} dq-axis PWM reference voltage.
V_{od}, V_{oq} DER LCL output voltage.
V_{sd}, V_{sq} dq-axis induction machine stator voltage.
V^*_{sd}, V^*_{sq} dq-axis induction machine stator voltage references.
V_{tri} Magnitude of PWM driver circuit triangular signal.
x_n Sampled state values of condition n.
$x_{01}, x_{02}, x_{03}, x_{end}$ Final states of prefault, fault, GFI and GSI stages time-domain analysis.
x_{tol} Time-domain analysis state tolerances.

Preprints (www.preprints.org) | NOT PEER-REVIEWED | Posted: 31 May 2020 doi:10.20944/preprints202005.0498.v1

and the type of load on FII stability is investigated by [1], the impact of inverter control-mode swiching delay and the demand/supply ratio is analyzed by [2], and the effect of different fault types is shown by [3].

Preliminary analysis has often considered microgrids with inertia from synchronous generators which serve as a frequency and phase angle reference immediately after islanding [1, 2, 3]. However, this leads to dynamics different from microgrids without synchronous generators, as respectively described for intentional islanding and larger networks by [9, 10]. In microgrids without inertia the inverter-based DERs have to create a frequency reference by switching from grid-feeding to grid-supporting control mode. Until now the stability phenomena in microgrids without inertia during the FII transient and especially the period between islanding and control-mode switching has not been analyzed in the literature.

Stability analysis of FII transients can be performed with time-domain simulations. Simulations of microgrid transients are commonly performed using component-based models [11] which have a high computational burden. This prohibits the time-critical stability analysis during operation of microgrids, which is required to determine the probability of successful islanding and perform control actions to improve this probability.

To decrease simulation time and also allow seperate small-signal and large-signal stability analyis, microgrid models in the dq reference frame have been proposed by [12, 13, 14, 15]. The microgrid dq models are validated for small-signal phenomena, however the validation for large-signal phenomena such as FII transients is still lacking in the literature.

The contributions of this paper are:

1. Proposition of a probabilistic stability analysis methodology to support planning and operation of FII microgrids without inertia.

2. Description and numerical validation of the stability phenomena and root causes for instability of microgrids without inertia during FII transients.

3. Description and numerical validation of the accuracy and computation time of dq microgrid models with inverter-based DERs, and static and dynamic load for FII simulations.

4. Demonstration of the probabilistic stability analysis methodology with a case study of a FII microgrid without inertia.

The stability phenomena and root causes for instability are described in the next section. In section 3 the stability analysis methodology, dq microgrid models and validation methodology are discussed. The results of the instability and dq model validation, and the case study are presented in section 4. In section 5 the results are discussed and finally conclusions are given in section 6.

2. FII Dynamics and Stability

The FII transient can be separated into different stages with unique dynamics. In this section, the dynamics during each stage are discussed in detail and finally an overview of the root causes of instability during each stage is shown in table 1. This paper uses the microgrid stability classifications as defined by [8] and DER control mode classifications as defined by [16]. The instability phenomena and root causes for instability discussed in this section are validated with simulations described in section 3.3.

2.1. FII sequence

A typical microgrid without inertia containing two inverter-based DERs and two types of loads is shown in figure 1. In this paper it is assumed that microgrids operate normally in grid-connected operation and switch to islanded operation after a fault has occurred in the external grid. In islanded operation, the grounding transformer located at the PCC provides grounding to the microgrid. During normal operation all DERs in the microgrid operate in grid-feeding control mode, as the main grid supplies the reference voltage and phase angle [16]. When a fault occurs in the external grid, the microgrid is in the fault stage and supplies a fault current until the fault is detected by the protection system located at the PCC. The protection system opens the PCC, islanding the microgrid. The microgrid is now in the grid-feeding islanding (GFI) stage without voltage and frequency reference. The microgrid remains in

Preprints (www.preprints.org) | NOT PEER-REVIEWED | Posted: 31 May 2020 doi:10.20944/preprints202005.0498.v1

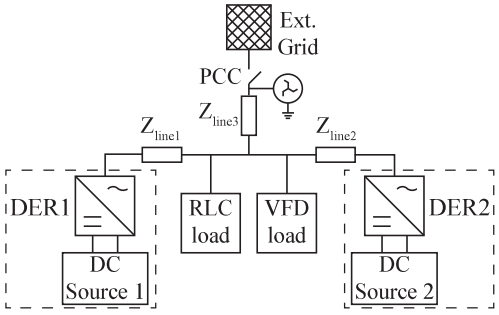

Figure 1: Generic microgrid with two DERs and two types of loads.

this stage until the islanding detection system of the DERs detect the islanding situation. When islanding is detected, the control mode of the DERs are switched from grid-feeding to grid-supporting operation. The microgrid is now in the grid-supporting islanding (GSI) stage where it will remain until the resynchronization sequence of the microgrid and the main grid is initiated.

Note that DERs can also operate in grid-supporting operation or as virtual synchronous generators during grid-connected operation to support the voltage and frequency of the main grid as discussed by [17]. In this case the GFI stage does not occur. However when DERs provide voltage and frequency support at all time, the self-governance of DER owners is strongly reduced. This prevents the DERs owners e.g. to maximize profit, to maintain a certain state of charge of energy storage systems or to maximize self-sufficiency during normal operation. Therefore, the DERs are assumed to normally operate in grid-feeding operation in the paper.

2.2. *Fault stage*

The duration of the fault stage depends on the operating time of the protection system, which is typically between 100ms and 600ms [18, 19]. During the fault stage, the voltage decreases and the DERs supply their limited fault current, and the DERs and load devices may drop-off depending on their fault-ride through (FRT) capabilities. The FRT capabilities of DERs are specified by the local grid-codes, while (power electronic) load devices switch off when the DC-link voltage reaches a critically low value [20]. DERs and load drop-off impacts the power balance in the microgrid, which can have a significant impact on the stability during the GFI and GSI stages.

2.3. *Grid-feeding islanding stage*

The duration of the GFI stage depends on the detection time of the islanding detection of the DERs, which is typically between 10ms and 2s depending on the type of islanding detection [21]. During the GFI stage, DERs attempt to inject power according to their active and reactive power references. If the power injected by the DERs is larger than the power absorbed by the load the voltage in the network will increase, and vice versa. This leads to voltage deviations from the nominal value which can cause DER and load drop-off.

During the GFI stage, the phase-locked loop (PLL) of the DERs has no phase angle reference. During this stage the PLL of the DERs interact with the load, causing the estimated frequency to drift from its nominal value depending on the properties of the PLL and the load [22]. This affects the frequency stability of the islanded microgrid as the frequency will increase when the load is dominantly inductive, while the frequency will decrease if the load is capacitive.

The PLL of the DERs can also fail to synchronize due to differences in bandwidth and/or structure of the PLLs, and due to the interactions with the load. This can cause large circulating currents between inverters, affecting converter stability in the microgrid.

The stability during the GFI stage is mainly impacted by the islanding detection time, DER power references, load properties (voltage sensitivity and power factor) and PLL properties.

2.4. *Grid-supporting islanding stage*

During the GSI stage, the voltage and frequency are controlled by the DERs in grid-supporting mode according to a power sharing strategy such as droop control [23].

Preprints (www.preprints.org) | NOT PEER-REVIEWED | Posted: 31 May 2020 doi:10.20944/preprints202005.0498.v1

Table 1: Root causes of instability for each FII stage and stability type.

Stability type	Fault	Grid-feeding islanding	Grid-supporting islanding
Control system stability	-	Large PLL bandwidth differences Low load power factor	Poorly tuned droop parameters Different islanding detection times
Power supply & balance stability	Fault characteristics	Imbalance of DERs power references and load power High load voltage sensitivity High PLL bandwidth Low load power factor	Insufficient DERs primary source power Large DERs or load drop-off Small DC-link capacitor

The grid-supporting DERs inject or absorb active and reactive power to control the voltage and frequency to near-nominal values. The primary source of the DERs (e.g. photovoltaics or battery energy storage) may have a lack of power generation capacity, causing the voltage of the DC-link capacitor to decrease. When this voltage decreases, the maximum output power of the DERs decrease which may cause voltage and/or frequency stability issues.

When DERs use droop control to ensure power sharing, circulating currents may occur between DERs when the droop parameters are poorly tuned. This causes oscillations in the network affecting converter stability in the microgrid [8].

Note that a situation with partly grid-feeding and partly grid-supporting DER can occur since not all DERs may be able to switch to grid-supporting operation or the islanding detection time may differ between DERs. In this case the PLL of grid-feeding and droop control of grid-supporting DERs may desynchronize, causing high circulating currents.

The stability during the GSI stage is mainly impacted by the power balance (DERs primary source power and load power), size of the DC-link capacitor, islanding detection time and droop control parameters.

3. Methodology

3.1. Stability analysis methodology

The conditions of the microgrid before FII are uncertain as faults can occur at any given time and the properties of microgrids are dynamic e.g. due to intermittent generation and changing network configuration and changing load level. As discussed in section 1, microgrid operators should analyze the FII stability while planning and periodically while operating of the microgrid. The probability of stable FII is determined in two steps. First the domain of operating conditions which result in stable islanding is determined with time-domain analysis. Second, the probability of the conditions lying within the stable domain is determined based on the probability distribution functions (PDFs) of the condition variables. During microgrid planning the PDFs are based on the expected conditions during the operation of the microgrid e.g. PV irradiation, load properties, while during microgrid operation the PDFs are based on forecast conditions. The generation of these PDFs is considered to be outside of the scope of this paper, therefore they are assumed to be known in advance.

As an input, the stability analysis methodology requires a set of time steps corresponding to the time horizon to evaluate $t \in T$, the minimum and maximum condition variable values $[x_{min}, x_{max}]$ which can occur over time T, microgrid models for each FII stage, and PDFs for each condition variable for each time step t. n values are created for each condition variable by interpolating between $[x_{min}, x_{max}]$ and all possible combinations of the interpolated values are stored in condition set N as shown in figure 2.

3.1.1. Planning and operation conditions

The conditions to be analyzed with the stability analysis methodology should reflect the expected operating conditions of the microgrid that may cause stability problems during FII. As discussed before the conditions during planning consist of a predefined set of expected conditions which are used to design the microgrid, while the conditions during operation consist of a set of forecast conditions.

As the root causes for instability are discussed in section 2, these can be used to determine the conditions which should be analyzed. As can be seen in table 1, the DER power references and primary source power, and the load power, power factor and voltage sensitivity are root causes for instability which vary over time. These condition

Preprints (www.preprints.org) | NOT PEER-REVIEWED | Posted: 31 May 2020 doi:10.20944/preprints202005.0498.v1

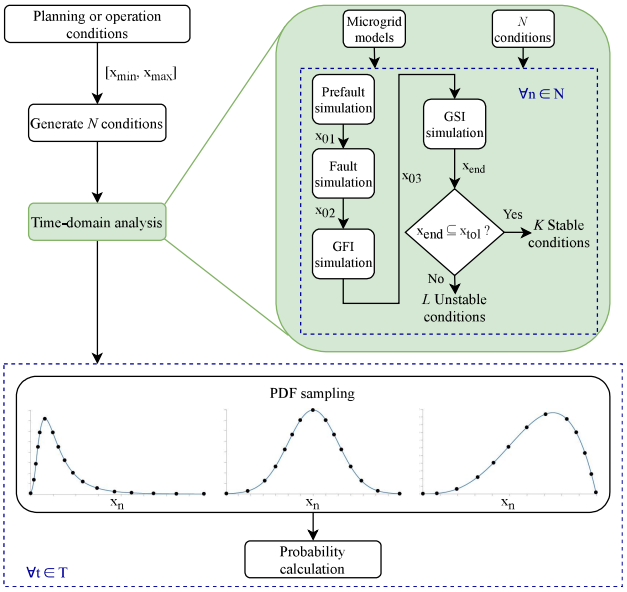

Figure 2: Overview of the stability analysis methodology. PDF:probability distribution function, GFI: grid-feeding islanding, GSI: grid-supporting islanding.

variables analyze possible control system, and power supply and balance instabilities caused by power imbalance, and interactions between PLLs and the load. The impact of the fault duration should also be analyzed, since a longer fault duration causes more drop-off of DERs and load which in turn impacts the power balance.

Note that in practical cases, not all parameters are exactly known while planning and operation of microgrids. Depending on the microgrid modeling uncertainty, additional conditions can be created with different PLL, droop and DC-link parameters to produce a robust stability verdict.

3.1.2. Time-domain analysis

Time-domain analysis of each condition $n \in N$ is performed to analyze under which conditions the microgrid is stable after FII. The analysis of each condition is initiated with the prefault simulation. The final states of the prefault simulation are used as the initial condition x_{01} of the fault stage simulation. The same procedure is executed with the GFI and GSI stages. The final states of the GSI stage x_{end} are compared to a set of state tolerances x_{tol} to determine if the condition is stable or unstable. The set x_{tol} is determined according to the fixed equilibrium point to which the system should converge during the GSI stage and a tolerance set by the user.

3.1.3. PDF sampling and probability calculation

The PDF of the output power of DERs depends on their type of primary source. The power generation of photovoltaic and wind powered DERs can be described by Beta and Weibull PDF respectively [24]. Load power and voltage sensitivity depends on the type of load devices, which can be described by lognormal distribution function [25]. The fault duration PDF depends on the type of protection device and the fault characteristics. The modeling uncertainty can be described with a gaussian PDF. The PDFs are sampled at values x_n as shown in figure 2. The probability of the condition n is described by $p_n = \prod_{i=1}^{I} p_i$. The probability of successful islanding is determined by the sum of the probability of all stable conditions $p_{ss} = \sum_{k=1}^{K} p_k$.

Depending on the probability of stability and the required FII reliability, the microgrid operator can decide to change the microgrid design, or control DERs or flexible load to improve the probability of stable islanding. During the planning phase of a microgrid there are many options to improve the probability of stable islanding since the design of DERs, loads and network can still be modified. In the operational phase the options are limited, however the state of charge of energy storage can be increased to increase the share of certain generation capacity, or demand-side management (DSM) can be applied to shift part of the load to a time with high renewable generation.

Preprints (www.preprints.org) | NOT PEER-REVIEWED | Posted: 31 May 2020 doi:10.20944/preprints202005.0498.v1

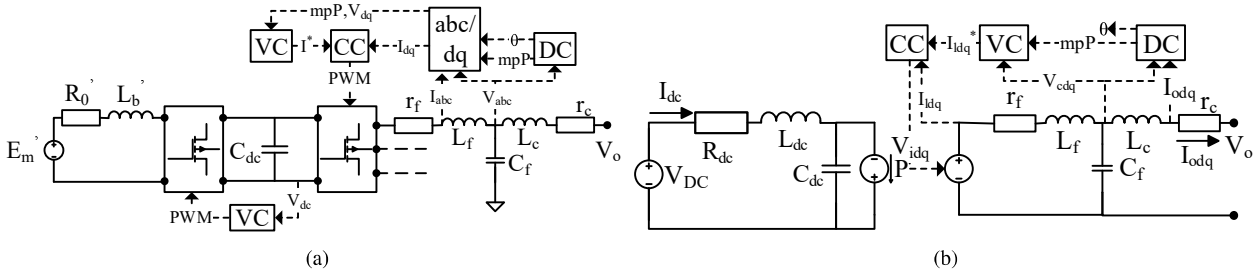

Figure 3: Model from [5] (a) and proposed dq (b) grid-supporting DER model. DC: droop controller. VC: voltage controller. CC: current controller.

3.2. *dq microgrid models*

To simulate FII transients, four dq microgrid models are developed: prefault, fault, GFI and GSI. Each microgrid model consists of grid-feeding DER, grid-supporting DER, parallel RLC load and variable frequency drive (VFD) load subsystems connected via an underground cable network. The subsystem models are created by transforming the component-based models described in [5] to the dq reference frame.

3.2.1. *dq Reference frame*

In the prefault and fault stage the frequency is dominantly determined by the external grid, therefore the frequency of the dq reference frame is equal to the external grid frequency ($\omega = \omega_n = 100\pi$). In the GFI stage the frequency is determined by the PLL of the DERs in the microgrid as described in section 2. The reference frame frequency is therefore equal to the frequency estimated by the PLL of DER1 ($\omega = \dot{\theta}_1$). In the GSI stage the frequency is determined by the droop controllers of the DERs in the microgrid. Therefore, the reference frame frequency is equal to the frequency calculated by the inverse droop controller of DER1 ($\omega = nq_1Q_1$).

3.2.2. *Grid-supporting DER*

The component-based grid-supporting DER and the dq grid-supporting DER model proposed in this paper are shown in figure 3. The boost converter is removed and the DC-link component parameters $E_m^{'}$, $R_0^{'}$ and $L_b^{'}$ are scaled to the nominal DC-link voltage as parameters V_{dc}, R_{dc} and L_{dc}, then the DC-link dynamics are described by equations 1. The three-phase inverter of the original model is replaced by a power source P and voltage source V_{idq} described by the inverse droop controller and equation 2 respectively, where $\omega_c = 10$rad/s and $\sqrt{V_{id}^2 + V_{iq}^2} \leq V_{tri}$. The inverse droop, voltage and current controllers are described by equations 3, 4 and 5, and 6 respectively. Finally, the lcl filter dynamics are described by equation 7. Note that a sigmoid function is added to equation 6 to represent the output current limit which is present is DER inverters.

$$\begin{bmatrix} \dot{I_{dc}} \\ \dot{V_{Cdc}} \end{bmatrix} = \begin{bmatrix} -\frac{R_{dc}}{L_{dc}} & -\frac{1}{L_{dc}} \\ \frac{1}{C_{dc}} & -\frac{P}{C_{dc}V_{Cdc}^2} \end{bmatrix} \begin{bmatrix} I_{dc} \\ V_{Cdc} \end{bmatrix} + \begin{bmatrix} \frac{V_{DC}}{L_{dc}} \\ 0 \end{bmatrix} \tag{1}$$

$$\begin{bmatrix} v_{id} \\ v_{iq} \end{bmatrix} = \begin{bmatrix} K_{ic}\zeta_d + K_{pc}\tilde{I_{ld}^*} - K_{pc}I_{ld} \\ K_{ic}\zeta_q + K_{pc}I_{lq}^* - K_{pc}I_{lq} \end{bmatrix} \tag{2}$$

$$\begin{bmatrix} \dot{\theta} \\ \dot{P} \\ \dot{Q} \end{bmatrix} = \begin{bmatrix} 0 & 0 & -nq \\ 0 & -\omega_c & 0 \\ 0 & 0 & -\omega_c \end{bmatrix} \begin{bmatrix} \theta \\ P \\ Q \end{bmatrix} + \begin{bmatrix} \omega_n - \omega \\ 1.5\omega_c(V_{cd}I_{od} + V_{cq}I_{oq}) \\ 1.5\omega_c(V_{cd}I_{oq} - V_{cq}I_{od}) \end{bmatrix} \tag{3}$$

$$\begin{bmatrix} \dot{\psi_d} \\ \dot{\psi_q} \end{bmatrix} = \begin{bmatrix} 0 \end{bmatrix} \begin{bmatrix} \psi_d \\ \psi_q \end{bmatrix} + \begin{bmatrix} -mpP + V_n - V_{cd} \\ -V_{cq} \end{bmatrix} \tag{4}$$

$$\begin{bmatrix} I_{ld}^* \\ I_{lq}^* \end{bmatrix} = \begin{bmatrix} K_{iv}\psi_d + K_{pv}(-mpP + V_n) - K_{pv}V_{cd} \\ K_{iv}\psi_q - K_{pv}V_{cq} \end{bmatrix} \tag{5}$$

Preprints (www.preprints.org) | NOT PEER-REVIEWED | Posted: 31 May 2020 doi:10.20944/preprints202005.0498.v1

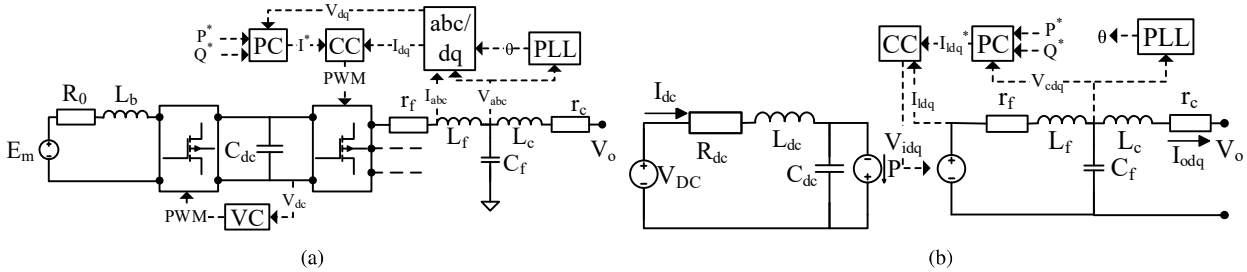

Figure 4: Model from [5] (a) and proposed dq (b) grid-feeding DER model. PC: power controller. CC: current controller. PLL: phase-locked loop.

$$\begin{bmatrix}\dot{\zeta}_d\\ \dot{\zeta}_q\end{bmatrix} = [0]\begin{bmatrix}\zeta_d\\ \zeta_q\end{bmatrix} + \begin{bmatrix}\tilde{I^*_{ld}} - I_{ld}\\ I^*_{lq} - I_{lq}\end{bmatrix}, \quad \tilde{I^*_{dq}} = \frac{I_{lim} I^*_{dq}}{\sqrt{I^2_{lim} + I^{*2}_{dq}}} \tag{6}$$

$$\begin{bmatrix}\dot{I}_{ld}\\ \dot{I}_{lq}\\ \dot{V}_{cd}\\ \dot{V}_{cq}\\ \dot{I}_{od}\\ \dot{I}_{oq}\end{bmatrix} = \begin{bmatrix}-\frac{r_f}{L_f} & \omega & -\frac{1}{L_f} & 0 & 0 & 0\\ -\omega & -\frac{r_f}{L_f} & 0 & -\frac{1}{L_f} & 0 & 0\\ \frac{1}{C_f} & 0 & 0 & \omega & -\frac{1}{C_f} & 0\\ 0 & \frac{1}{C_f} & -\omega & 0 & 0 & -\frac{1}{C_f}\\ 0 & 0 & \frac{1}{L_c} & 0 & -\frac{r_c}{L_c} & \omega\\ 0 & 0 & 0 & \frac{1}{L_c} & -\omega & -\frac{r_c}{L_c}\end{bmatrix}\begin{bmatrix}I_{ld}\\ I_{lq}\\ V_{cd}\\ V_{cq}\\ I_{od}\\ I_{oq}\end{bmatrix} + \begin{bmatrix}\frac{v_{id}V_I}{L_f}\\ \frac{v_{iq}V_I}{L_f}\\ 0\\ 0\\ -\frac{v_{od}}{L_c}\cos(\theta) - \frac{v_{oq}}{L_c}\sin(\theta)\\ \frac{v_{od}}{L_c}\sin(\theta) - \frac{v_{oq}}{L_c}\cos(\theta)\end{bmatrix}, \quad V_I = \frac{V_{Cdc}}{2V_{tri}} \tag{7}$$

3.2.3. *Grid-feeding DER*

The grid-feeding DER model is similar to the grid-supporting DER model as they are the same devices with different controllers as shown in figure 4. The grid-feeding DER model consists of equations 1, 6, 2 and 7 from the grid-supporting DER model. As opposed to droop control, grid-feeding DER rely on a PLL to determine the phase angle as described by equation 8. The output power reference determines the output current as described by equation 9.

$$\begin{bmatrix}\dot{\gamma}\\ \dot{\theta}\end{bmatrix} = \begin{bmatrix}0 & 0\\ K_{ipll} & 0\end{bmatrix}\begin{bmatrix}\gamma\\ \theta\end{bmatrix} + \begin{bmatrix}V_{cq}\\ K_{ppll}V_{cq} + \omega_n - \omega\end{bmatrix} \tag{8}$$

$$\begin{bmatrix}I^*_{ld}\\ I^*_{lq}\end{bmatrix} = \begin{bmatrix}\frac{2P^*}{3V_{cd}}\\ \frac{2Q^*}{3V_{cd}}\end{bmatrix} \tag{9}$$

3.2.4. *Parallel RLC load*

The dynamics of the parallel RLC load are described by equation 10 in terms of the voltage of the capacitor and the current through the inductor.

$$\begin{bmatrix}\dot{V}_{Cld}\\ \dot{V}_{Clq}\\ \dot{I}_{Lld}\\ \dot{I}_{Llq}\end{bmatrix} = \begin{bmatrix}\frac{-1}{R_l C_l} & \omega & \frac{-1}{C_l} & 0\\ -\omega & \frac{-1}{R_l C_l} & 0 & \frac{-1}{C_l}\\ \frac{1}{L_l} & 0 & 0 & \omega\\ 0 & \frac{1}{L_l} & -\omega & 0\end{bmatrix}\begin{bmatrix}V_{Cld}\\ V_{Clq}\\ I_{Lld}\\ I_{Llq}\end{bmatrix} + \begin{bmatrix}\frac{I_{bd}}{C_l}\\ \frac{I_{bq}}{C_l}\\ 0\\ 0\end{bmatrix} \tag{10}$$

3.2.5. *Variable frequency drive load*

The component-based VFD load model and the dq VFD model proposed in this paper are shown in figure 5. The three-phase rectifier of the original model is replaced by a transformer, where $S_d = \frac{3}{2}\frac{2\sqrt{3}}{\pi}$ as described by [26]. The DC-link dynamics are then described by equation 11. The three-phase inverter is replaced by voltage source $V_{sd} = \frac{V_{Cdc}}{2V_{tri}}V^*_{sd}$, $V_{sq} = \frac{V_{Cdc}}{2V_{tri}}V^*_{sq}$ and a power source $P_e = \frac{3}{2}(V_{sd}I_{sd} + V_{sq}I_{sq})$. The speed and direct torque controllers are described by equation 13. The synchronous reference frame induction motor model is described by [27].

Preprints (www.preprints.org) | NOT PEER-REVIEWED | Posted: 31 May 2020 doi:10.20944/preprints202005.0498.v1

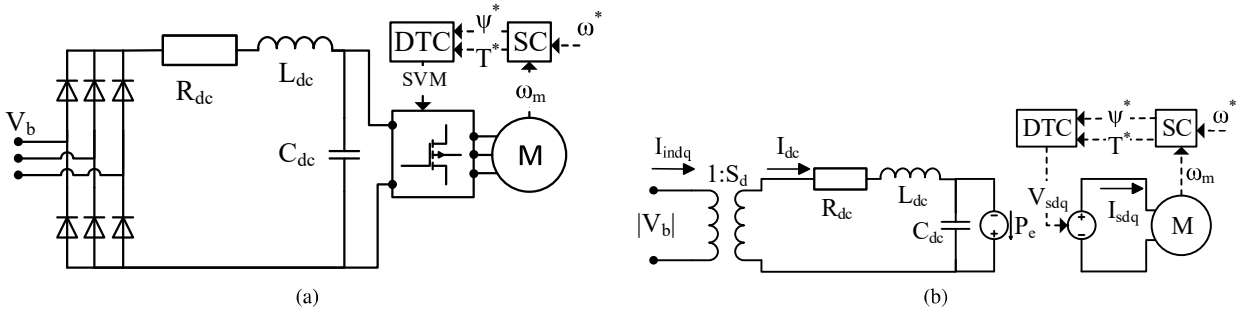

Figure 5: Model from [5] (a) and proposed dq (b) variable frequency drive model. DTC: direct torque controller. SC: speed controller.

$$\begin{bmatrix} \dot{I_{dc}} \\ \dot{V_{Cdc}} \end{bmatrix} = \begin{bmatrix} -\frac{R_{dc}}{L_{dc}} & -\frac{1}{L_{dc}} \\ \frac{1}{C_{dc}} & -\frac{P_e}{C_{dc}V_{Cdc}^2} \end{bmatrix} \begin{bmatrix} I_{dc} \\ V_{Cdc} \end{bmatrix} + \begin{bmatrix} \sqrt{\frac{3}{2}}\frac{2\sqrt{3}}{\pi L_{dc}}|V_b| \\ 0 \end{bmatrix} \tag{11}$$

$$\begin{bmatrix} V_{sd}^* \\ V_{sq}^* \end{bmatrix} = \begin{bmatrix} K_{pf}\psi^*\alpha - K_{pf}\sqrt{\psi_{sd}^2 + \psi_{sq}^2} \\ K_{pt}\tilde{T}^*\alpha + K_{it}\phi_q - \frac{3pK_{pt}I_{sq}}{2}\psi_{sd} + \frac{3pK_{pt}I_{sd}}{2}\psi_{sq} \end{bmatrix} \tag{12}$$

$$\begin{bmatrix} \dot{\phi_q} \\ \dot{\delta} \end{bmatrix} = \begin{bmatrix} 0 \end{bmatrix} \begin{bmatrix} \phi_q \\ \delta \end{bmatrix} + \begin{bmatrix} \tilde{T}^*\alpha + \frac{3}{2}pI_{sd}\psi_{sq} - \frac{3}{2}pI_{sq}\psi_{sd} \\ \omega^* - \omega_m \end{bmatrix}, \quad \tilde{T}^* = T_{lim}\frac{K_{i\omega}\delta + K_{p\omega}(\omega^* - \omega_m)}{\sqrt{T_{lim}^2 + (K_{i\omega}\delta + K_{p\omega}(\omega^* - \omega_m))^2}} \tag{13}$$

Variable α is used to model drop-off behavior of the VFD load. DC-link undervoltage leads to temporary drop-off, therefore $\alpha = 0$ when $V_{Cdc} \leq 327$V and $\alpha = 1$ when $V_{Cdc} \geq 351$V (due to hysteresis). Permanent drop-off occurs when the rotational speed of the induction motor is equal to zero, therefore $\alpha = 0$ when the rotational speed is equal to zero ($\omega_m = 0$rad/s). The current absorbed by the VFD load $I_{ind} = S_d I_{dc}\cos(\sigma)$, $I_{inq} = S_d I_{dc}\sin(\sigma)$, where $\sigma = \arctan(\frac{V_{bq}}{V_{bd}})$. ψ_{sd}, ψ_{sq} are the d-axis and q-axis stator flux, $T_{lim} = 75$Nm, $\psi^* = \psi_n$, $V_{Cdc} > 0$, $\sqrt{V_{sd}^{*2} + V_{sq}^{*2}} \leq V_{tri}$ and $I_{dc} \geq 0$.

3.2.6. *Network*

The network is modeled as series RL branches. The current through the branch is described by equation 14.

$$\begin{bmatrix} \dot{I_{lined}} \\ \dot{I_{lineq}} \end{bmatrix} = \begin{bmatrix} -\frac{R_{line}}{L_{line}} & \omega \\ -\omega & -\frac{R_{line}}{L_{line}} \end{bmatrix} + \begin{bmatrix} \frac{V_{bid} - V_{bjd}}{L_{line}} \\ \frac{V_{biq} - V_{bjq}}{L_{line}} \end{bmatrix} \tag{14}$$

3.3. *Validation of instability phenomena and dq microgrid model*

To validate the FII instability phenomena described in section 2 and the dq models described in section 3.2, FII simulations are performed of the network shown in figure 1. The results of the simulations using the dq models are compared to simulation results using previously validated component-based models described in [5]. The parameters indicated as the root causes for instability as described in table 1 are varied in the simulations.

In the base scenario the RLC load has a resistance, inductance and capacitance of 10.6Ω, 505mH and 20.1μF, and the VFD drives a mechanical constant torque load of 20Nm. The 50mm^{2}Al underground cables 1, 2 and 3 are 100m, 150m and 50m long respectively with an impedance of $Z_{line} = 0.71 + 0.075j\frac{\Omega}{\text{km}}$. The duration of the fault and GFI stages depend on the fault and islanding detections times respectively as described in section 2. The fault and islanding detection times are both assumed to be 0.2s, while the total simulation time is 1s. The active and reactive power inverse droop parameters of both DERs are $mp_{1,2} = \frac{8.125}{10}\frac{\text{V}}{\text{kW}}$ and $nq_{1,2} = \frac{0.1\pi}{10}\frac{\text{rad/s}}{\text{kVAr}}$ respectively, the proportional and integral voltage controller gains are $k_{pv} = 0.37$ and $k_{iv} = 241$ respectively, the power of the DC sources is 10kW and the DC-link capacitors of the DERs have a rating of 0.5mF. All other model parameters of the grid-supporting DER, grid-feeding DER and VFD load devices are determined in [5]. The grid-feeding active power reference of both DERs is 7.5kW. All scenarios use the same parameters as the base scenario, unless specified otherwise.

Preprints (www.preprints.org) | NOT PEER-REVIEWED | Posted: 31 May 2020 doi:10.20944/preprints202005.0498.v1

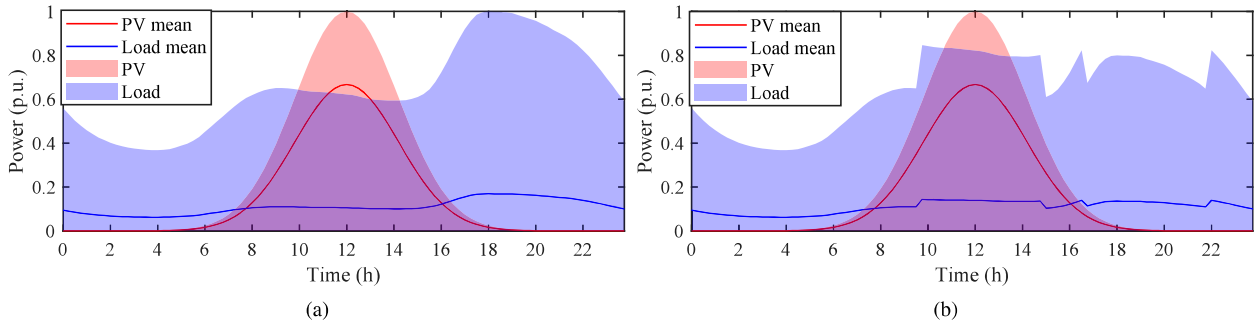

Figure 6: Probability distribution function and their mean of PV and load power over time in the case study before (a) and after (b) shifting load with DSM.

In scenario GFI1 the resistance and capacitance of the RLC load are increased to 31.7Ω, 401μF, and the proportional, integral controller gains of the PLL of DER1 and DER2 are $K_{ppll1} = 10$, $K_{ipll1} = 500$ and $K_{ppll2} = 200$, $K_{ipll2} = 10000$ respectively. In scenario GFI2 the resistance and capacitance of the RLC load are increased to 63.5Ω, 401μF and the active power reference of both DER is decreased to 5kW.

In scenario GSI1 the load torque and the drop-off voltage of the VFD are changed to 50Nm and 220V. Scenario F is equal to scenario GSI1 where the fault stage duration and total simulation time are increased by 0.2s. In scenario GSI2 the DC-link capacitance of both DERs is reduced to 100μF, the power calculation low-pass filter bandwidth $\omega_c = 5$rad/s, and the active, reactive droop parameters of DER 1 and 2 are $mp_1 = \frac{16.25}{1}\frac{\text{V}}{\text{kW}}$ and $nq_1 = \frac{0.2\pi}{1}\frac{\text{rad/s}}{\text{kVAr}}$ and $mp_2 = \frac{40.625}{1}\frac{\text{V}}{\text{kW}}$ and $nq_2 = \frac{0.5\pi}{1}\frac{\text{rad/s}}{\text{kVAr}}$ respectively. In scenario GSI3 the islanding detection time of DER2 is increased by 0.2s, inductance of the RLC load is decreased to 25.3mH, and the PI controller gains of the PLL of DER2 are five times larger.

3.4. Microgrid planning and operation case study

The planning and operation of the network shown in figure 1 is treated in the case study of this paper. The probability of stable islanding is analyzed over a day, representing either the planning conditions or a day-ahead forecast during operation of the microgrid. The condition variables in the case study consist of the PV output power and the load. DER1 is a battery energy storage system and DER2 is a PV generation system both with a nominal power of 10kW. The microgrid parameters are equal to the base scenario described in section 3.3. The PV output power varies between 0kW and 10kW, and is modeled by changing the output power reference and resistance of the primary source of DER2. The RLC and VFD loads vary between 0kW, 20kW and 0Nm and 70Nm respectively, modeled by changing the RLC impedance and the load torque.

To determine the stability boundaries 11 values are created for the PV and load condition variables by interpolating between the minimum and maximum values, resulting in a total of 121 different conditions. Time-domain analysis of all conditions are performed using the dq microgrid models. As instabilities are reflected in the voltage and frequency in the network, these states can be used to detect instable conditions. The voltage, frequency and VFD rotational speed state tolerances x_{tol} are 32.5V, 1Hz and 10rad/s respectively. As described in section 3.1.1 the output power of the PV is described by a Beta distribution with parameters $\alpha_\beta = 4, \beta_\beta = 2$, while the power absorbed by the RCL load and VFD is described by a Lognormal distribution with parameters $\mu_{log} = 0, \sigma_{log} = 0.69$. The PV and load profiles are shown in figure 6 (a), where the mean of the load is based on the average of the E1A (household demand) load profile defined by [28].

To analyze the impact of DSM on the probability of stable islanding, 20% of the load power during 17h-22h is shifted to 10h-15h. This results in a lower load during the evening and a higher load around noon when the probability of PV generation is high as shown in figure 6 (b).

To analyze the impact of the energy storage device rating on the probability of stable islanding, the case study is analyzed with different DER1 power ratings. The power rating of DER1 is increased to 15kVA by modifying the resistance of the primary source of DER 1 R_0.

Preprints (www.preprints.org) | NOT PEER-REVIEWED | Posted: 31 May 2020 doi:10.20944/preprints202005.0498.v1

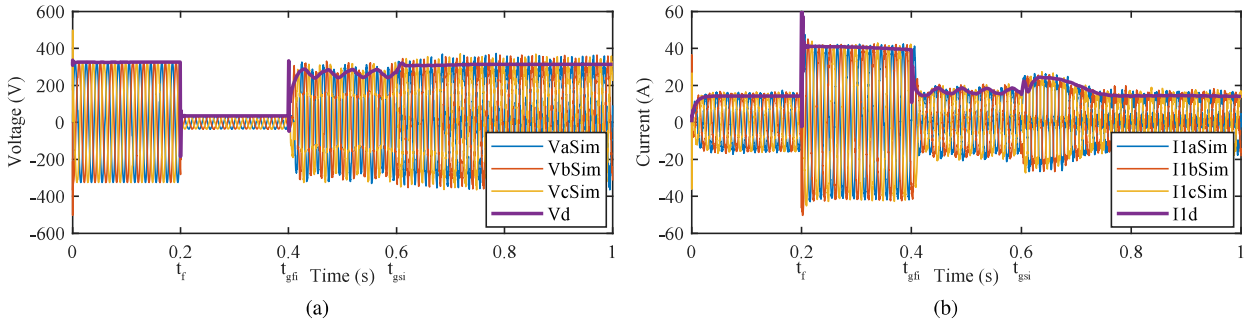

Figure 7: Voltage at the load (a) and output current (b) of DER1 of component-based and dq models in base scenario.

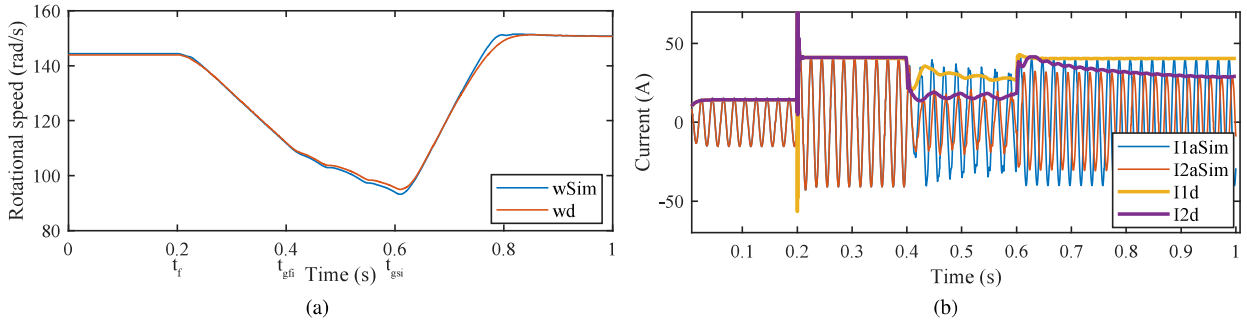

Figure 8: Rotational speed of the component-based and dq VFD induction machine models in base scenario (a) and output current of DER1 and DER2 of component-based and dq models in GFI1 scenario (b).

4. Results

4.1. Instability and dq model validation

The voltage and current during FII of the component-based (denoted by $_{a,b,cSim}$) and d-axis component of the dq models (denoted by $_{d}$) in the base scenario are shown in figures 7 (a) and (b) respectively. The initiation of the fault, GFI and GSI stages are denoted by t_f, t_{gfi} and t_{gsi}. During the fault stage, the voltage decreases which causes the DERs supply a high current depending on the fault current limit. Due to the low voltage the VFD drops-off which causes the rotational speed to decrease as shown in figure 8(a). The voltage recovers to a lower than nominal value during the GFI stage as the total load is larger than the DER power references. Finally, the voltage recovers during the GSI stage which causes the VFD rotational speed to increase to above the nominal value and slowly decreases to the nominal value.

The output current of the DERs in scenario GFI1 is shown in figure 8(b). The different PLL bandwidth causes the PLLs of the DERs to estimate a different phase angle during the GFI stage, which is accelerated by the low power factor of the RLC load. The phase angle difference leads to control system instability visible as high circulating current during the GFI and GSI stages.

In scenario GFI2 a large frequency deviation from nominal occurs during the GFI stage due to interactions between the PLLs of the DERs and the load as shown in figure 9(a). The load is dominantly capacitive which causes the frequency to decrease during the GFI stage to approximately 29Hz. The network frequency during the FII transient using component-based and dq models is shown in figure 10.

The voltage in scenario GSI1 is shown in figure 9 (b). The power absorbed by the load is higher than the DER power output, causing power supply & balance instability visible as low network voltage. The low voltage causes the VFD to continuously drop-off, which increases the voltage until the VFD recovers which in turn decreases the voltage.

When the fault duration is increased in scenario F, the rotational speed of the VFD reaches zero and permanent drop-off occurs. This causes the voltage to remain stable during the GFI and GSI stages in scenario F as shown in

Preprints (www.preprints.org) | NOT PEER-REVIEWED | Posted: 31 May 2020 doi:10.20944/preprints202005.0498.v1

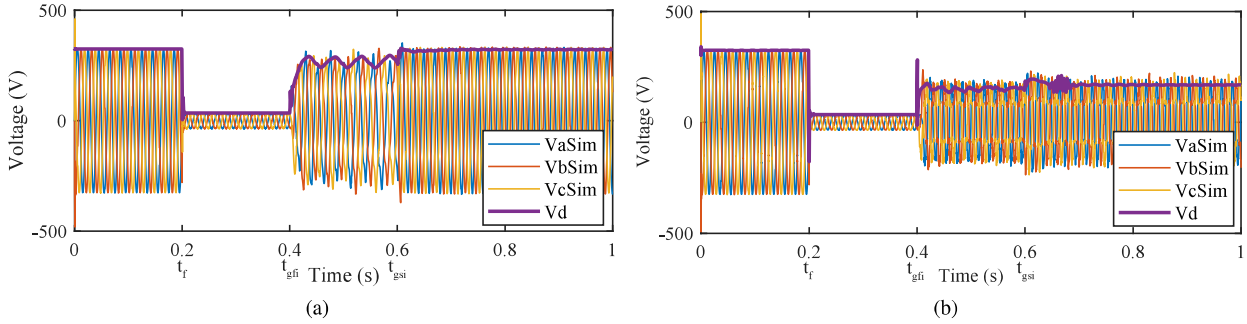

Figure 9: Voltage at the load of component-based and dq models in GFI2 scenario (a) and GSI1 scenario (b).

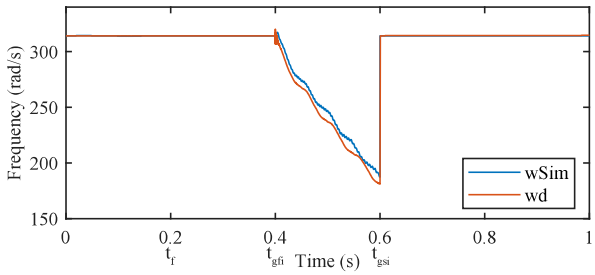

Figure 10: Network frequency in microgrid using component-based models and the proposed dq models in scenario GFI2.

figure 11(a).

The larger droop controller parameters cause the phase angles of the DERs to desynchronize during the GSI phase in scenario GSI2 as shown in figure 11(b). This causes control system instability visible as high circulating current.

When 0.6s $\leq t <$ 0.8s in scenario GSI3, the droop controller of DER1 and the PLL of DER2 fail to synchronize causing a high circulating current and a voltage dip during the GSI stage. After control-mode switching of DER2 at t = 0.8s the DERs fail to synchronize, resulting in a high circulating current and a low network voltage as shown in figures 12 (a) and (b).

The simulation time of the validation scenarios with component-based models is between 1193 and 1525 seconds, while the simulation time with the proposed dq models is between 18 and 25 seconds. As the simulation time is 98% to 99% smaller when the proposed dq models are used, this allows a large set of conditions to be analyzed to support network operators during microgrid operation.

4.2. Microgrid planning and operation case study

Out of the 121 tested conditions in the case study, 83 and 72 conditions resulted in instability with a DER1 power rating of 10kVA and 15kVA respectively when the load power was high compared to the generation capacity.

The stability results of the case study for different DER1 power ratings are visualized in figure 13 together with probability contour plots indicating the probability of the PV and load power at t = 12:00 and t = 17:00. The probability contour plots indicate what conditions have the highest probability as described by the PDFs of the PV and load, with the inner ring being the conditions with the highest probability.

At t = 12:00 the probability of the condition variables being in the stable domain is much higher than being in the unstable domain, while at t = 17:00 a larger part of the probability contours are within the unstable domain. Note that the probability contours are different at each time step, while the stability boundaries are independent of the time step. A higher rating of DER1 increases the size of the stable domain and therefore increases the probability of the conditions being stable.

The probability of stable FII over the day with and without DSM for different DER1 power ratings is shown in figure 14. As the generation capacity of the microgrid strongly depends on the intermittent PV generation, the islanding capability greatly varies over the day without DSM. In the case with a DER1 rating of 10kVA and without

Preprints (www.preprints.org) | NOT PEER-REVIEWED | Posted: 31 May 2020 doi:10.20944/preprints202005.0498.v1

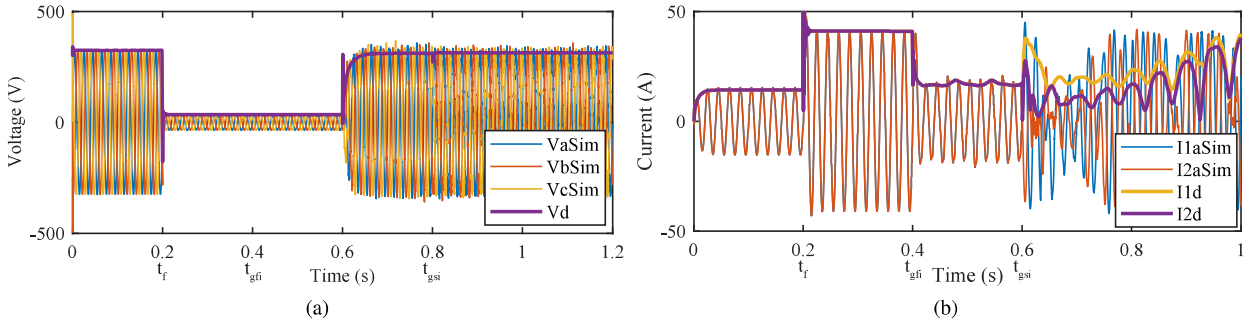

(a) (b)

Figure 11: Voltage at the load in F scenario (a) and output current of DER1 and DER2 in scenarios GSI2 (b) of component-based and dq models.

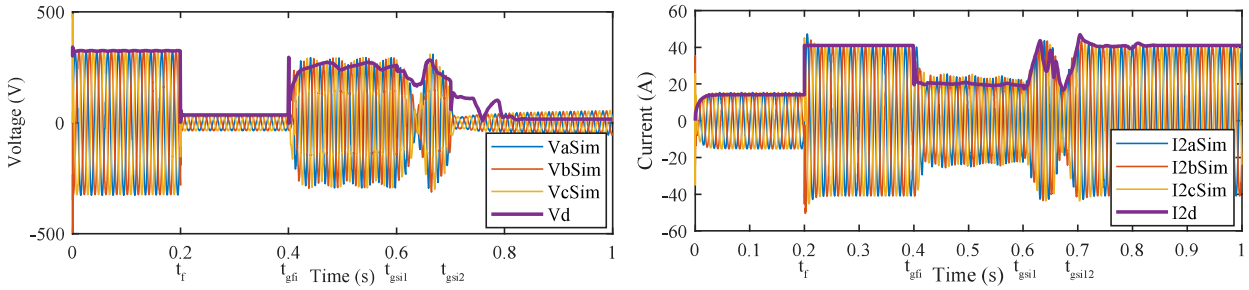

(a) (b)

Figure 12: Voltage at the load (a) and output current of DER 2 of component-based and dq models in GSI3 scenario (b). t_{gsi1}: DER1 control-mode switching, t_{gsi2}: DER2 control-mode switching.

DSM, the probability of stable islanding up to 15:45 is between 92% and 97% due to the small load in the morning and high PV around noon. In the afternoon and evening the probability drops to 57% due to high load and low PV generation.

When DSM is applied the load is shifted from a period with low PV generation to a period with high PV generation. This significantly increases the probability of stable islanding in the afternoon and evening is to over 80%, while the probability around noon is slightly decreased. When the power rating of DER1 is increased to 15kVA the generation capacity in the microgrid is higher and less volatile. As shown in figure 14 (b) this drastically increases the probability of stable islanding over the day.

Each condition was simulated for 2 seconds to determine stability. The total computation time of the 121 conditions is between 704 and 727 seconds using an Intel Xeon E5-2670 and 16GB of RAM.

5. Discussion

The description and validation of the stability phenomena which can occur during and right after FII provides new insights, which are an addition to the analysis performed in [1, 2, 3, 8]. Desynchronization which can occur between PLLs, and between the PLL and droop controllers of DERs during the islanding transient has not been identified before. Additionally, the impact of load drop-off, and interactions between the PLL of DERs and the load on the stability during the islanding transient have also not been investigated before. Different instability phenomena may arise during resynchronization of the microgrid with the main grid, which will be analyzed in future research.

As can be seen from the model validation results, the dq model significantly reduces the computation time compared to the component-based models, while accurately representing the magnitude and frequency of the states of the microgrid even during large voltage and frequency transients, or desynchronization of DERs as shown in scenarios base, GFI1, GFI2 and GSI1. During severe desynchronization of DERs the dq model is not able to accurately represent

Preprints (www.preprints.org) | NOT PEER-REVIEWED | Posted: 31 May 2020 doi:10.20944/preprints202005.0498.v1

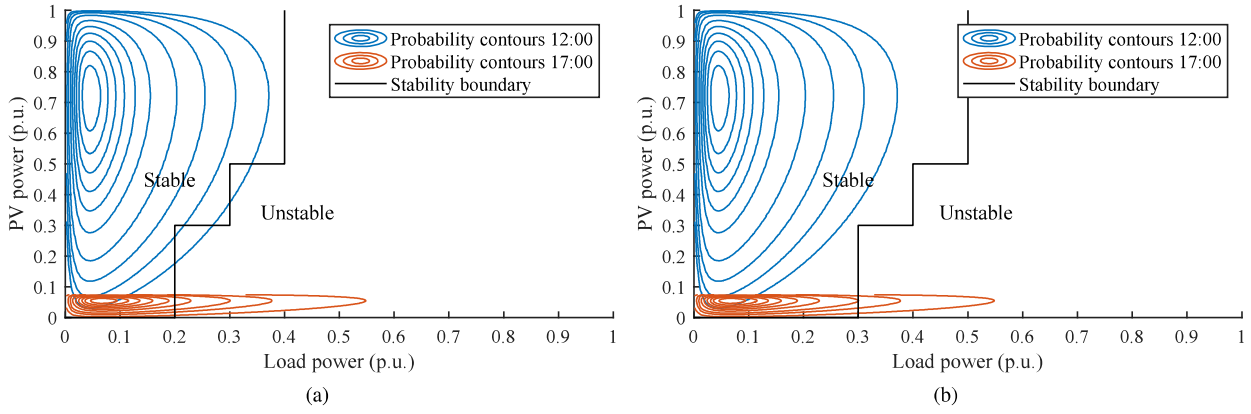

Figure 13: Case study stability boundary, and probability contours of PV and load condition variables at t = 12:00 and t = 17:00 for DER1 ratings of 10kVA (a) and 15kVA (b).

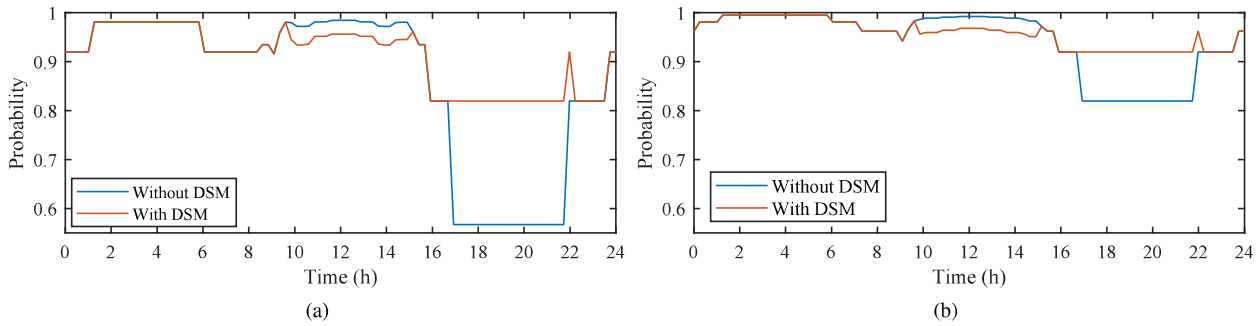

Figure 14: Probability of stable FII over the day with and without shifted load by demand-side management (DSM) for DER1 ratings of 10kVA (a) and 15kVA (b).

behavior, however the instabilities are visible in the dq model as shown in scenarios GSI2 and GSI3. This validates the dq microgrid models to detect the instabilities which can occur during FII. However, dq models inherently cannot be (directly) used for the analysis of unbalanced microgrids or detect harmonic instability phenomena. To include harmonics and analyze unbalanced situations, the models can be extended to dynamic phasor models [29].

The total computation time of the case study indicates that the proposed stability analysis can be performed in near real-time, allowing the network operator to use it for both planning and operation decisions. As the proposed stability analysis methodology generates a probability of stable islanding, these decisions can be based on a quantified cost-benefit analysis. As shown in the case study, both DSM and changing the energy storage rating can be used to increase the probability of stable islanding. The cost of load shifting and increasing the DER rating can be compared to the cost of an outage. Future research should investigate the options to improve the probability of stable islanding and perform detailed cost-benefit analysis of larger microgrids.

6. Conclusion

Fault-initiated islanding microgrids can improve the reliability of the electrical energy supply. The probabilistic stability analysis methodology is proposed in this paper allows microgrid operators to make microgrid design choices and take control actions based on quantified probabilistic results. The root causes for FII instability described in the paper can be used to identify critical unstable conditions and to validate the FII capability of microgrids. The dq models proposed in the paper are compared to previously validated component-based models and show high accuracy while significantly reducing the computation time.

Future research should investigate the instability phenomena during resynchronization with the main grid, cost-benefit analysis of FII microgrids, and the application of dynamic phasor models to analyze harmonics and unbalance.

Acknowledgement

This work has received funding from the European Union's Horizon 2020 research and innovation program under grant agreement No 773717.

References

[1] A. H. Kasem Alaboudy, H. H. Zeineldin, J. Kirtley, Microgrid stability characterization subsequent to fault-triggered islanding incidents, IEEE Transactions on Power Delivery 27 (2) (2012) 658–669. doi:10.1109/TPWRD.2012.2183150.

[2] W. Zheng, P. Crossley, B. Xu, H. Qi, Transient stability of a distribution subsystem during fault-initiated switching to islanded operation, International Journal of Electrical Power and Energy Systems 97 (August 2017) (2018) 418–427. doi:10.1016/j.ijepes.2017.11.024.
URL https://doi.org/10.1016/j.ijepes.2017.11.024

[3] F. Katiraei, M. R. Iravani, P. W. Lehn, Micro-grid autonomous operation during and subsequent to islanding process, IEEE Transactions on Power Delivery 20 (1) (2005) 248–257. doi:10.1109/TPWRD.2004.835051.

[4] M. H. Roos, P. H. Nguyen, J. Morren, J. G. Slootweg, Sectionalizing Distribution Networks Concept and System Framework, in: 2018 International Conference on Smart Energy Systems and Technologies (SEST), IEEE, 2018, pp. 1–6. doi:10.1109/SEST.2018.8495731.
URL https://ieeexplore.ieee.org/document/8495731/

[5] M. H. Roos, P. H. Nguyen, J. Morren, J. G. Slootweg, Modeling and Experimental Validation of Power Electronic Loads and DERs For Microgrid Islanding Simulations, IEEE Transactions on Power Systems 35 (3) (2020) 2279–2288. doi:10.1109/TPWRS.2019.2953757.
URL https://ieeexplore.ieee.org/document/8902151/

[6] X. Tang, W. Deng, Z. Qi, Investigation of the dynamic stability of microgrid, IEEE Transactions on Power Systems 29 (2) (2014) 698–706. doi:10.1109/TPWRS.2013.2285585.

[7] N. Bottrell, M. Prodanovic, T. C. Green, Dynamic stability of a microgrid with an active load, IEEE Transactions on Power Electronics 28 (11) (2013) 5107–5119. doi:10.1109/TPEL.2013.2241455.

[8] M. Farrokhabadi, C. A. Canizares, J. W. Simpson-Porco, E. Nasr, L. Fan, P. Mendoza-Araya, R. Tonkoski, U. Tamrakar, N. D. Hatziargyriou, D. Lagos, R. W. Wies, M. Paolone, M. Liserre, L. Meegahapola, M. Kabalan, A. H. Hajimiragha, D. Peralta, M. Elizondo, K. P. Schneider, F. Tuffner, J. T. Reilly, Microgrid Stability Definitions, Analysis, and Examples, IEEE Transactions on Power Systems 8950 (APRIL) (2019) 1–1. doi:10.1109/tpwrs.2019.2925703.

[9] I. J. Balaguer, Q. Lei, S. Yang, U. Supatti, F. Z. Peng, Control for Grid-Connected and Intentional Islanding Operations of Distributed Power Generation, IEEE Transactions on Industrial Electronics 58 (1) (2011) 147–157. doi:10.1109/TIE.2010.2049709.
URL http://ieeexplore.ieee.org/document/5462910/

[10] F. Milano, F. Dorfler, G. Hug, D. J. Hill, G. Verbic, Foundations and Challenges of Low-Inertia Systems (Invited Paper), in: 2018 Power Systems Computation Conference (PSCC), IEEE, 2018, pp. 1–25. doi:10.23919/PSCC.2018.8450880.
URL https://ieeexplore.ieee.org/document/8450880/

[11] JOINT WORKING GROUP C4/C6.35/CIRED, Modelling of Inverter- Based Generation for Power System Dynamic Studies, Tech. Rep. May, CIRED (2018).

[12] Y. Levron, J. Belikov, Modeling power networks using dynamic phasors in the dq0 reference frame, Electric Power Systems Research 144 (2017) 233–242. doi:10.1016/j.epsr.2016.11.024.
URL http://dx.doi.org/10.1016/j.epsr.2016.11.024

[13] E. S. Raju P, T. Jain, Impact of load dynamics and load sharing among distributed generations on stability and dynamic performance of islanded AC microgrids, Electric Power Systems Research 157 (2018) 200–210. doi:10.1016/j.epsr.2017.12.022.
URL http://dx.doi.org/10.1016/j.epsr.2017.12.022

[14] D. Baimel, J. Belikov, J. M. Guerrero, Y. Levron, Dynamic Modeling of Networks, Microgrids, and Renewable Sources in the dq0 Reference Frame: A Survey, IEEE Access 5 (2017) 21323–21335. doi:10.1109/ACCESS.2017.2758523.

[15] M. Rasheduzzaman, J. A. Mueller, J. W. Kimball, An accurate small-signal model of inverter-dominated islanded microgrids using (dq) reference frame, IEEE Journal of Emerging and Selected Topics in Power Electronics 2 (4) (2014) 1070–1080. doi:10.1109/JESTPE.2014.2338131.

[16] J. Rocabert, A. Luna, F. Blaabjerg, P. Rodríguez, Control of Power Converters in AC Microgrids, IEEE Transactions on Power Electronics 27 (11) (2012) 4734–4749. arXiv:arXiv:1011.1669v3, doi:10.1109/TPEL.2012.2199334.
URL http://ieeexplore.ieee.org/document/6200347/

[17] H. Bevrani, T. Ise, Y. Miura, Virtual synchronous generators: A survey and new perspectives, International Journal of Electrical Power and Energy Systems 54 (2014) 244–254. doi:10.1016/j.ijepes.2013.07.009.
URL http://dx.doi.org/10.1016/j.ijepes.2013.07.009

[18] H. Laaksonen, D. Ishchenko, A. Oudalov, Adaptive protection and microgrid control design for Hailuoto Island, IEEE Transactions on Smart Grid 5 (3) (2014) 1486–1493. doi:10.1109/TSG.2013.2287672.

[19] O. Núñez-Mata, R. Palma-Behnke, F. Valencia, P. Mendoza-Araya, G. Jiménez-Estévez, Adaptive protection system for microgrids based on a robust optimization strategy, Energies 11 (2) (2018). doi:10.3390/en11020308.

[20] Cirgré Working Group C4.605, Modelling and Aggregation of Loads in Flexible Power Networks, Tech. Rep. February, Cigre (2014).

[21] C. Li, C. Cao, Y. Cao, Y. Kuang, L. Zeng, B. Fang, A review of islanding detection methods for microgrid, Renewable and Sustainable Energy Reviews 35 (2014) 211–220. doi:10.1016/j.rser.2014.04.026.

[22] D. Dong, B. Wen, D. Boroyevich, P. Mattavelli, Y. Xue, Analysis of Phase-Locked Loop Low-Frequency Stability in Three-Phase Grid-Connected Power Converters Considering Impedance Interactions, IEEE Transactions on Industrial Electronics 62 (1) (2015) 310–321. doi:10.1109/TIE.2014.2334665.
URL http://www.ams.org/jourcgi/jour-getitem?pii=S0002-9939-10-10151-8 http://ieeexplore.ieee.org/document/6848832/

[23] Y. Han, H. Li, P. Shen, E. A. A. Coelho, J. M. Guerrero, Review of Active and Reactive Power Sharing Strategies in Hierarchical Controlled Microgrids, IEEE Transactions on Power Electronics 32 (3) (2017) 2427–2451. doi:10.1109/TPEL.2016.2569597.

[24] M. Aien, M. G. Khajeh, M. Rashidinejad, M. Fotuhi-Firuzabad, Probabilistic power flow of correlated hybrid wind-photovoltaic power systems, IET Renewable Power Generation 8 (6) (2014) 649–658. doi:10.1049/iet-rpg.2013.0120.

[25] A. K. Ghosh, D. L. Lubkeman, M. J. Downey, R. H. Jones, Distribution circuit state estimation using a probabilistic approach, IEEE Power Engineering Review 17 (2) (1997) 46–47.

[26] K. N. Areerak, S. V. Bozhko, G. M. Asher, D. W. Thomas, Stability analysis and modelling of AC-DC system with mixed load using DQ-transformation method, IEEE International Symposium on Industrial Electronics (2008) 19–24doi:10.1109/ISIE.2008.4676898.

[27] P. Kundur, Power System Stability and Control, McGraw-Hill Education, New York, 1994.
URL http://www.scirp.org/journal/doi.aspx?DOI=10.4236/wjm.2014.46018

[28] NEDU, Verbruiksprofielen Elektriciteit 2020 (2019).
URL https://www.nedu.nl/documenten/verbruiksprofielen/

[29] Z. Shuai, Y. Peng, J. M. Guerrero, Y. Li, Z. J. Shen, Transient Response Analysis of Inverter-Based Microgrids under Unbalanced Conditions Using a Dynamic Phasor Model, IEEE Transactions on Industrial Electronics 66 (4) (2019) 2868–2879. doi:10.1109/TIE.2018.2844828.